Modelling of Internal Fluid Flow in Cracks with Embedded Strong Discontinuities

Mijo Nikolic, Adnan Ibrahimbegovic and Predrag Miscevic

Abstract This chapter presents a discrete approach for modelling failure of heterogeneous rock material with discrete crack propagation and internal fluid flow through the saturated porous medium, where the coupling conditions between the solid and fluid phase obey the Biot's porous media theory. Discrete cracks and localized failure mechanisms are provided through the concept of embedded discontinuity FEM. Furthermore, the basis for presented discrete 2D plane strain model representation of heterogeneous material consisting of material grains, is an assembly of Voronoi cells that are kept together by cohesive links in terms of Timoshenko beams. Embedded discontinuities are built in cohesive links thus providing the discontinuity propagation between the rock grains in mode I and mode II. The model can also take into account the fracture process zone with pre-existing microcracks coalescence prior to the localized failure. Several numerical simulations are given to illustrate presented discrete approach.

1 Introduction

Cracks and other localized failure mechanisms in rocks and other heterogeneous materials represent the dominant failure mechanisms, which occur often in civil engineering practice like in dam failure, foundation collapse, stability of excava-

M. Nikolic
LMT Cachan, École Normale Supérieure de Cachan, 61 Avenue du Président Wilson,
94230 Cachan, France
e-mail: mijo.nikolic@gradst.hr

M. Nikolic · P. Miscevic
University of Split, FCEAG Split, Matice hrvatske 15, 21000 Split, Croatia
e-mail: predrag.miscevic@gradst.hr

A. Ibrahimbegovic (✉)
Laboratoire Roberval de Mecanique, Centre de Recherche Royallieu,
Chair for Computational Mechanics, Sorbonne Universitès/UT Compiègne,
60200 Compiègne, France
e-mail: adnan.ibrahimbegovic@utc.fr

tions, slopes and tunnels, landslides and rock falls. The risk of localized failure should be better understood in order to be prevented. The localized failure in rocks is usually characterized by a sudden and brittle failure without warning in a sense of larger and visible deformations prior to failure. This happens also under the strong influence of material heterogeneities, pre-existing cracks and other defects. Numerical modelling represents a main approach in engineering design and research with the the simulations standing as significant tool for obtaining more insight into the full control of material behaviour.

The fluid flow through deformable porous rock medium additionally modifies its mechanical properties and failure response. Two coupling mechanisms play the key role in the fluid-structure interaction problem of this kind: the first concerns the influence of of pore pressure increase inducing the material dilation, and the second pertains to compressive mechanical stress leading to an increase of a pore pressure and making the material less compliant than in the fully-drained case. This problem has received a great attention in engineering literature. The elastic and (homogenized) plastic hardening response was addressed in pioneering works of Terzaghi and Biot [1, 2] and in more recent contribution [3].

Proper modeling of localized failure demands different approach than continuum approach used in usual engineering tasks, where Finite Element Method (FEM) has been considered as the main tool for solving vast majority of applications [4–6]. In order to provide a reliable predictive model for failure of rocks, the discontinuous solutions should be found, where pre-existing cracks continue to form into new ones during the increased loading leading to failure. The evolution of crack patterns shows that localization is a key factor inducing brittle failure. Thus, the main challenge tackled is to provide enhanced predictive models for localized failure by taking into account the material heterogeneities and pre-existing cracks.

Two notable enhanced methods derived from the standard framework of Finite Element Method (FEM) to deal with localization, i.e. cracks, discontinuities. The first one is the Finite Element Method with Embedded Discontinuities (ED-FEM), representing cracks truly in each element (e.g. see [7–10]). The second one is Extended Finite Element Method (X-FEM) where cracks are represented globally [11–13]. The same methods have been used recently for simulating the localized failure when fluid flows through the porous domain. Namely, X-FEM has been used in simulating hydraulic fracturing of fully-saturated [14] and partially-saturated [15] porous media with cohesive cracks, as well as in saturated shear band formations [16]. The fluid saturated poro-elastic and poro-plastic medium with localized failure zones have been simulated with ED-FEM in [17, 18], while the partially saturated medium can be found in [19]. Another approach for simulating the failure of porous fractured media is with automatic mesh refinement process presented in [20], which was also extended to 3D situation in [21].

This chapter presents an approach for modelling the localized failure in rocks under the influence of heterogeneities and pre-existing defects like found in [22, 23]. The class of discrete lattice models have been chosen for general framework of the numerical model that have been previously used in simulating the progressive failure of concrete and rocks [24]. Namely, the basis of this framework is in representation
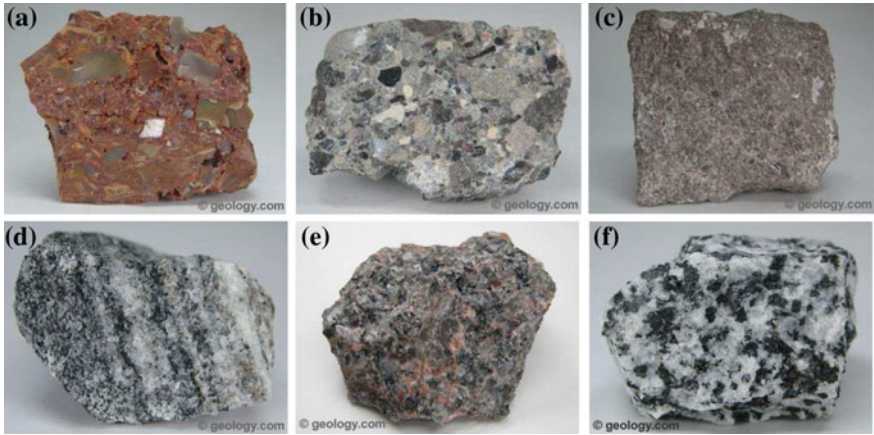
Fig. 1 Grainy structure of different rocks: **a** breccia (sedimentary), **b** conglomerate (sedimentary), **c** limestone (sedimentary), **d** gneiss (metamorphic), **e** granite (igneous), **f** quartz-diorite (igneous). The size of all of the samples is approximately 5 cm. The photographs are taken from http://geology.com/rocks/

of heterogeneous material which is considered as assembly of grains of material held together by cohesive links. This framework corresponds also to the geological formation of rocks, where many different groups of rocks possess a grainy structure which allows the grain recognition even with the bare eye (Fig. 1).

Rock domain is discretized with the Voronoi cells representing rock grains, while Timoshenko beams act as cohesive links between them (Fig. 2).

Several papers developed discrete lattice models, where the domain is discretized with the Voronoi cells [25, 26].

Fig. 2 The basis of the proposed discrete model relies on the lattice of Timoshenko beams which represent the cohesive links keeping the rock grains (Voronoi cells) together
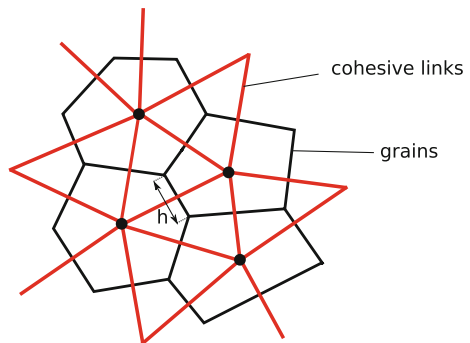
Usually, the discrete lattice models simulate the progressive failure characterized by localization with re-meshing process [27]. Namely, the cohesive links are sequentially removed from the mesh when the discontinuity propagate between the grains. The main difference in the presented model, with respect to latter approach, concerns embedded discontinuities placed within the framework of ED-FEM, where Timoshenko beam elements are equipped with enhanced kinematics capable of capturing the localization effects, like shown in [28–30]. Namely, the embedded discontinuities are placed in the middle of each Timoshenko beam. This corresponds to the Voronoi cell network, where each cohesive link is cut by half by the edge between two neighbouring Voronoi cells.

The embedded discontinuity in the longitudinal local direction of cohesive link (Timoshenko beam) enables the grain dilation due to mode I or tensile failure mode. However, Timoshenko beams also allow to account for pronounced shear effects in both elastic and plastic phase which is used here for representing the failure in mode II (shear sliding along the grains) adding the corresponding displacement or strong discontinuity in the transversal local direction. This leads to localized solutions (i.e. discontinuity propagations) which are enabled like shown in Fig. 3.

Heterogeneities are considered through two different phases representing the initial state; the intact rock material and the initial weaker material that stands for pre-existing defects. The macroscopic response of the system is largely influenced by the distribution and position of the phases. The intact rock material is represented by the stronger links, (i.e. Timoshenko beams). Thus, the discontinuity is more likely to propagate through the weaker phase. Failure of the material can occur in both modes separately, as well as in their combination.

Fig. 3 The strong discontinuity propagation between the Voronoi cells invokes the enhanced kinematics activation
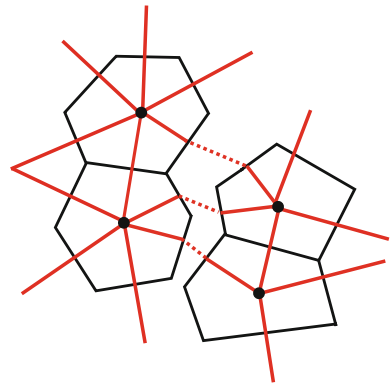
applied fluid pressure

grains
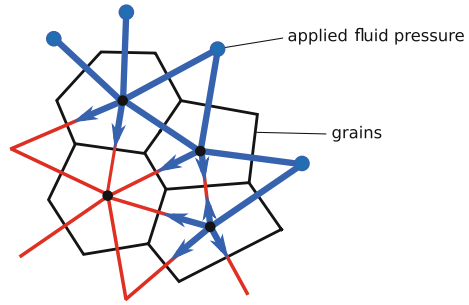
> Fluid flow through the saturated porous domain is governed by a diffusion equation incorporating the Darcy law in terms of continuous pore pressures across the discrete lattice domain (Fig. 4), like shown in [18, 19, 31].

Fluid flow is spread across the lattice of beams, where fluid pressure acts as additional degree of freedom of the beam. The coupled process between the mechanics strain and fluid flow in deformable medium with micro-cracks is governed by Biot's porous media theory [2].

2 Numerical Model Formulations

Rock is considered as porous solid saturated with a fluid. The flow conditions allows that convective terms and gravity acceleration be neglected in this problem. Standard equilibrium equation of saturated two-phase medium is given by relation

$$\nabla \cdot \sigma = 0, \tag{1}$$

where the total stress is

$$\sigma = \sigma_s + \sigma_f = \sigma' - bp \tag{2}$$

and subscripts s and f denote the solid and the fluid part, respectively. The effective stress $\sigma_s = \sigma'$ measures the material properties of the solid skeleton under drained conditions, p is fluid pressure and b is Biot coefficient. Fluid equation is given with

$$\frac{1}{M}\frac{\partial p}{\partial t} + b\nabla \cdot v_s + \nabla \cdot v_f = 0, \tag{3}$$

where vectors v_s and v_f represent the velocities of the solid and the fluid, respectively. The latter is defined by the Darcy law

$$v_f = -k_f \nabla p \tag{4}$$

where k_f is the permeability of the porous medium, M is Biot's modulus defined as

$$\frac{1}{M} = \frac{n_f}{K_f} + \frac{b - n_f}{K_s}, \tag{5}$$

and b is a Biot coefficient defined as

$$b = 1 - \frac{K_t}{K_s}. \tag{6}$$

Here, n_f denotes porosity, K_f is the bulk modulus of the fluid, K_s is a bulk modulus of the solid and K_t is the overall bulk modulus of the porous medium.

The presented model is based on Timoshenko beam elements connecting the grains of material in terms of Voronoi cells. Thus, the weak form of the equilibrium equation (1), in terms of stress resultant (Timoshenko beams) states

$$\int_0^{l_e} \frac{d\mathbf{w}}{dx} \sigma \, dx = \int_0^{l_e} \mathbf{w} \mathbf{f} dx + \mathbf{w} \mathbf{F}, \tag{7}$$

where $\sigma = [N \; T \; M]^T$ represents the stress resultant vector, $\mathbf{f} = [f \; q \; m]^T$ is the distributed load vector and $\mathbf{F} = [F \; Q \; C]^T$ is the vector of concentrated forces. The right hand side in (7) provides the vector of external forces $\mathbf{F}^{ext}$ with the standard finite element manipulations. The vector $\mathbf{w}$ represents a virtual generalized displacements $V_0 = \{\mathbf{w} : [0, l_e] \mapsto R \; | \; [\mathbf{w}]_{\Gamma_u} = 0\}$, which ought to be differentiable and verify $\mathbf{w} \in V_0$.

The constitutive relations for the porous medium (2) are given in terms of total stresses, effective stresses and pore pressures $\sigma = \sigma' - b\mathbf{p}$. The total stress in terms of stress resultants can be decomposed into

$$\begin{bmatrix} N \\ T \\ M \end{bmatrix} = \begin{bmatrix} N' \\ T' \\ M' \end{bmatrix} - b \begin{bmatrix} pA \\ 0 \\ 0 \end{bmatrix}, \tag{8}$$

where the effective stress resultant components can be obtained through the solid's skeleton 'drained' elasticities denoted with $\mathbf{D}_{sk}$

$$\begin{bmatrix} N' \\ T' \\ M' \end{bmatrix} = \underbrace{\begin{bmatrix} EA & 0 & 0 \\ 0 & GA & 0 \\ 0 & 0 & EI \end{bmatrix}}_{\mathbf{D}_{sk}} \begin{bmatrix} \varepsilon \\ \gamma \\ \kappa \end{bmatrix}. \tag{9}$$

Note that E represents Young's modulus, G shear modulus and I moment of inertia of the beam.

The fluid flow equation (3) takes the weak form for the discrete lattice representation of the domain

$$-\int_0^{l_e} \pi M^{-1} \frac{dp}{dt} dx + \int_0^{l_e} \frac{d\pi}{dx} \alpha \mathbf{v}_s dx$$
$$+ \int_0^{l_e} \frac{d\pi}{dx} k_f \frac{dp}{dx} dx = Q^{ext}, \tag{10}$$

where π is the virtual pressure field that obeys the same regularity as the virtual displacement field.

2.1 Enhanced Kinematics

This section provides the enhanced formulation for Timoshenko beam as cohesive link, resulting with embedded discontinuities in local longitudinal direction for mode I failure, and in transversal direction for mode II failure. The localized failure is accompanied by a softening regime in a global macro-response, where the heterogeneous displacement field is used in order to obtain a mesh-independent response. The formulation for fracture process zone with micro-cracks is also presented here through the hardening regime with standard plasticity.

The localization implies heterogeneous displacement field which no longer remains regular, even for smooth stress field. Thus, the displacement field ought to be introduced and written as the sum of a sufficiently smooth, regular part and a discontinuous part. Furthermore, the axial and transversal displacement fields need to be calculated independently.

A cohesive link finite element with two nodes of length l_e and cross section A is considered (Fig. 5). The standard degrees of freedom at each node $i \in [1, 2]$ are axial displacement u_i, transversal displacement v_i and rotation θ_i, accompanied with pressure p_i degree of freedom. The strain measures for standard Timoshenko element are given

$$\varepsilon(x) = \frac{du(x)}{dx}$$
$$\gamma(x) = \frac{dv(x)}{dx} - \theta(x) \tag{11}$$
$$\kappa(x) = \frac{d\theta(x)}{dx}.$$

In order to obtain the displacement jumps in the interiors of the cohesive links, the displacement fields need to be enhanced leading to regular and singular parts, where latter can be represented as a product of Heaviside function and displacement jump. The enhanced displacement fields can thus be written as

Fig. 5 The enhanced finite element with it's degrees of freedom and discontinuous shape function $M(x)$ and it's derivative $G(x)$
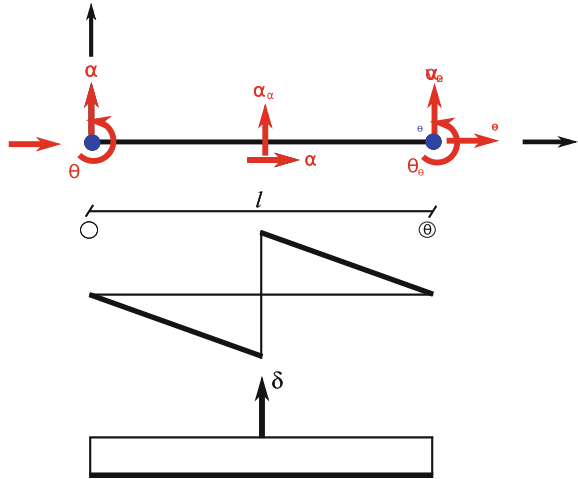
$$u(x) = \bar{u}(x) + \alpha_u H_{x_c}$$
$$v(x) = \bar{v}(x) + \alpha_v H_{x_c}, \tag{12}$$

where α_u and α_v represent incompatible mode parameters which denote the displacement jumps in axial and transversal direction providing the failure modes I and II. H_{x_c} is the Heaviside function being equal to one if $x > x_c$, and zero otherwise, while x_c is the position of the discontinuity. The presented model assumes the position of discontinuity to be in the middle of the beam. This is the case when each cohesive link is cut in half by the two neighboring Voronoi cells.

The enhanced deformation fields, in terms of regular and singular parts, results from (12) with

$$\varepsilon(x) = \bar{\varepsilon}(x) + \alpha^{(u)} \delta_{x_c}$$
$$\gamma(x) = \bar{\gamma}(x) + \alpha^{(v)} \delta_{x_c}, \tag{13}$$

where $\bar{\varepsilon}$ and $\bar{\gamma}$ denote regular parts, and Dirac delta δ_{x_c} is the singular part representation of the deformation field. The Dirac delta function δ_{x_c} takes an infinite value at $x = x_c$ and remains equal to zero everywhere else.

For this element, standard linear interpolation functions are used for regular displacement approximation

$$\mathbf{N} = \left\{ N_1(x) = 1 - \frac{x}{l_e}; \quad N_2(x) = \frac{x}{l_e} \right\}, \tag{14}$$

along with their derivatives

$$\mathbf{B} = \left\{ B_1(x) = -\frac{1}{l_e}; \quad B_2(x) = \frac{1}{l_e} \right\}. \tag{15}$$

Beside standard interpolations, the enhanced interpolation function M is derived in the spirit of ED-FEM (see [6, 22, 23]) and can be used alongside standard interpolation functions to describe the heterogeneous displacement fields with activated discontinuity jump producing embedded discontinuity inside the finite element. The $M(x)$ is defined as

$$M(x) = \begin{cases} -\frac{x}{l_e}; & x \in [0, x_c) \\ 1 - \frac{x}{l_e}; & x \in \langle x_c, l_e] \end{cases}, \tag{16}$$

while $G(x)$ represents the derivative of enhanced function $M(x)$, with respect to local coordinate direction x

$$\begin{aligned} G(x) &= \overline{G} + \delta_{x_c} \\ &= -\frac{1}{l_e} + \delta_{x_c}, \quad x \in [0, l_e]. \end{aligned} \tag{17}$$

Enhanced functions M and G are shown in Fig. 5. This kind of formulation cancels the contribution of incompatible mode parameter on the element boundary leading to possibility of computing the discontinuity parameters locally, while the global equations remain with the nodal displacements as primal unknowns.

Finally, the enhanced finite element displacement interpolations are written in terms of embedded discontinuity

$$\begin{aligned} u(x) &= \sum_{a=1}^{2} N_a(x)u_a + M(x)\alpha_u \\ v(x) &= \sum_{a=1}^{2} N_a(x)v_a + M(x)\alpha_v \\ \theta(x) &= \sum_{a=1}^{2} N_a(x)\theta_a. \end{aligned} \tag{18}$$

The discrete approximation of deformation field can be obtained from the above displacement field (18) resulting with

$$\begin{aligned} \varepsilon(x) &= \sum_{a=1}^{2} B_a(x)u_a + G(x)\alpha_u \\ \gamma(x) &= \sum_{a=1}^{2} (B_a(x)v_a - N_a(x)\theta_a) + G(x)\alpha_v \\ \kappa(x) &= \sum_{a=1}^{2} B_a(x)\theta_a, \end{aligned} \tag{19}$$

The fluid flow is enabled by adding the pressure degree of freedom on top of standard Timoshenko degrees of freedom leading to enhanced element, not only in terms of added pressures, but also in localized discontinuity contributions. The enhanced finite element with all degrees of freedom is shown in Fig. 5.

The pressure field is interpolated with the linear shape functions as well $\{N_1^P(x) = 1 - \frac{x}{l_e}, \quad N_2^P(x) = \frac{x}{l_e}\}$. The corresponding derivatives are $\{B_1^P(x) = -\frac{1}{l_e}, \quad B_2^P(x) = \frac{1}{l_e}\}$. However, the pressure interpolation functions are denoted with the superscript p for clearer presentation. Since the fluid flow problem is transient, the time parameter t is introduced and the discretization field for pressure follows

$$p(x, t) = \sum_{a=1}^{2} N_a^P(x) p_a(t). \tag{20}$$

The discretization of the pressure gradient is

$$\frac{\partial p}{\partial x}(x, t) = \sum_{a=1}^{2} B_a^P(x) p_a(t), \tag{21}$$

while its time derivative

$$\frac{\partial p}{\partial t}(x, t) = \sum_{a=1}^{2} N_a^P(x) \dot{p}_a(t). \tag{22}$$

The generalized nodal pressure field can be denoted with $\mathbf{p} = (p_1, p_2)^T$.

2.2 The Enhanced Weak Form

The generalized virtual deformations are interpolated in the same way as the real ones

$$\delta\boldsymbol{\varepsilon} = \mathbf{B}\delta\mathbf{d} + G\delta\boldsymbol{\alpha}, \tag{23}$$

with δ standing for prefix indicating the corresponding virtual field or variation. Such interpolated fields produce the internal force vector and the finite element residual vector due to discontinuity

$$\mathbf{F}^{int} = \int_0^{l_e} \mathbf{B}^T \boldsymbol{\sigma} \, dx,$$
$$\mathbf{h}^{(e)} = \int_0^{l_e} (\overline{G} + \delta_{x_c}) \boldsymbol{\sigma} \, dx. \tag{24}$$

From the condition of residual equation being equal to zero, the internal forces at the discontinuity ought to be calculated

$$\mathbf{h}^{(e)} = \int_0^{l_e} (\overline{G} + \delta_{x_c})\boldsymbol{\sigma}\,dx$$

$$= \int_0^{l_e} \overline{G}\boldsymbol{\sigma}\,dx + \mathbf{t}. \tag{25}$$

Vector $\mathbf{t}$ represents the internal forces at discontinuity, which are in relation with the forces from the bulk

$$\mathbf{t} = -\int_0^{l_e} \overline{G}\boldsymbol{\sigma}\,dx, \quad \mathbf{t} = (t_u, t_v, 0)^T \tag{26}$$

2.3 Constitutive Model

It has been observed that representative behaviour of rock material, including the post-peak behaviour, can be separated into five different stages based upon stress-strain characteristics. These stages can be defined as: crack closure, linear elastic deformation, crack initiation and stable crack growth, critical energy release and unstable crack growth, failure and post-peak behaviour. Figure 6 shows typical stress-strain curve of the brittle rock under the compression test and its failure stages.
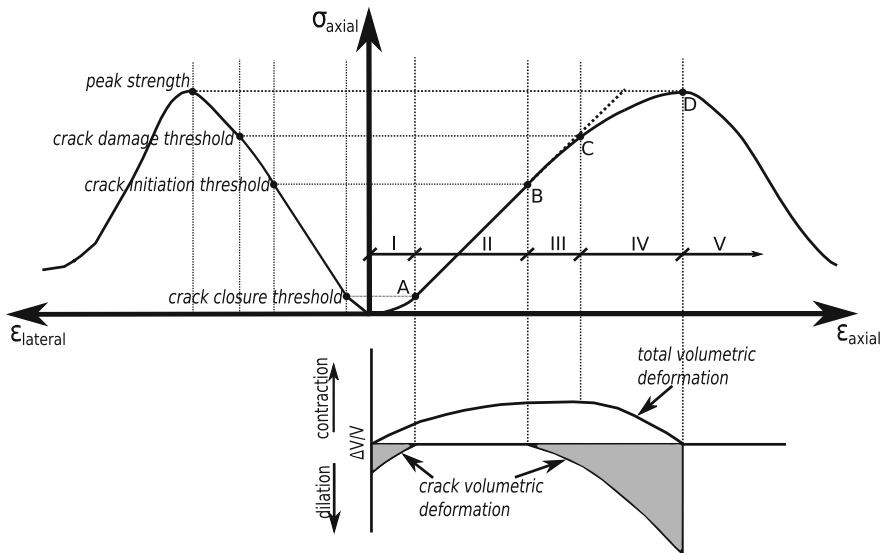

Fig. 6 Stress-strain curve showing the elements of crack development

Stage I is associated to microcrack closure and the initial flaws in the material which continues with stage II, a linear elastic stage. The inelastic behaviour starts at the beginning of stage III and until the end of stage, the hardening response accompanied by fracture process zone with microcrack initiation, can be observed. With an increase of a loading program, stage IV is activated. The stress value at the beginning of this stage (point C) can vary between 50–90% of ultimate strength, while the rest of the stage is characterized by the nonlinear behaviour and more rapid increase of lateral deformation. At the point D, the ultimate strength of specimen is reached and the larger macro-cracks start to propagate through the sample leading to softening of the specimen. At this point, the volumetric strain starts to reverse from a compressive to dilatation behaviour.

The constitutive relations need to be defined outside and at the discontinuity. The constitutive models are constructed within the framework of thermodynamics for a stress resultant beam formulation.

The beam longitudinal and transversal directions are enhanced with additional kinematics, representing modes I and II with softening behaviour, while the rotations keep their standard elastic form. The first two stages of rock failure (up to point B) are kept elastic, with respect to stage I being finished soon after the loading is applied. The linear elastic behaviour is finished when the point B is reached, continuing with hardening. When stage III is activated, significant damage caused by micro-crack propagation starts to occur in the specimen and increases until the highest peak point (point D). The constitutive model for latter stages, which represents a fracture process zone, is chosen as classical plasticity model with isotropic hardening. When the critical point is reached, the complete failure of the specimen is enabled through the exponential softening law. This invokes the enhanced kinematics activation and occurrence of the displacement jumps. The carrying capacity of element reduces with increase in the displacement jump.

In the following equations, the development for the failure of the beam in modes I and II is presented. When the loading starts and softening has not formed yet, the classical elasto-plastic model is considered. The total strains can be additively decomposed into elastic and plastic components

$$
\begin{aligned}
\varepsilon &= \overline{\varepsilon}^e + \overline{\varepsilon}^p \\
\gamma &= \overline{\gamma}^e + \overline{\gamma}^p.
\end{aligned}
\tag{27}
$$

Strain energy functions depend upon elastic strains and hardening variables, $\overline{\overline{\xi}}_u, \overline{\overline{\xi}}_v$:

$$
\begin{aligned}
\psi_u\left(\varepsilon, \overline{\varepsilon}^p, \overline{\overline{\xi}}_u\right) &= \frac{1}{2}EA\left(\varepsilon - \overline{\varepsilon}^p\right)^2 + \frac{1}{2}\overline{\overline{\xi}}_u^2 \overline{K}_u \\
\psi_v\left(\gamma, \overline{\gamma}^p, \overline{\overline{\xi}}_v\right) &= \frac{1}{2}GA\left(\gamma - \overline{\gamma}^p\right)^2 + \frac{1}{2}\overline{\overline{\xi}}_v^2 \overline{K}_v,
\end{aligned}
\tag{28}
$$

where $\overline{K}_u$ and $\overline{K}_v$ denote isotropic hardening modulus for longitudinal and transversal direction. The yield criterion is defined as

$$
\begin{aligned}
\overline{\Phi}_u\left(N, \overline{q}_u\right) &= N - \left(N_y - \overline{q}_u\right) \leq 0 \\
\overline{\Phi}_v\left(T, \overline{q}_v\right) &= |T| - \left(T_y - \overline{q}_v\right) \leq 0,
\end{aligned}
\tag{29}
$$

where N_y and T_y represent the forces at yielding point. The state equations are

$$
\begin{aligned}
N &= EA\left(\varepsilon - \overline{\varepsilon}^p\right) \\
T &= GA(\gamma - \overline{\gamma}^p).
\end{aligned}
\tag{30}
$$

and

$$
\begin{aligned}
\overline{q}_u &= -\overline{K}_u \overline{\xi}_u \\
\overline{q}_v &= -\overline{K}_v \overline{\xi}_v.
\end{aligned}
\tag{31}
$$

For the inelastic case, the principle of maximum dissipation is considered, the evolution laws are obtained as

$$
\begin{aligned}
\dot{\overline{\varepsilon}}^p &= \dot{\overline{\lambda}}_u \frac{\partial \overline{\Phi}_u}{\partial N} = \dot{\overline{\lambda}}_u sign(N); \quad \dot{\overline{\xi}}_u = \dot{\overline{\lambda}}_u \frac{\partial \overline{\Phi}_u}{\partial \overline{q}_u} = \dot{\overline{\lambda}}_u \\
\dot{\overline{\gamma}}^p &= \dot{\overline{\lambda}}_v \frac{\partial \overline{\Phi}_v}{\partial T} = \dot{\overline{\lambda}}_v sign(T); \quad \dot{\overline{\xi}}_v = \dot{\overline{\lambda}}_v \frac{\partial \overline{\Phi}_v}{\partial \overline{q}_v} = \dot{\overline{\lambda}}_v,
\end{aligned}
\tag{32}
$$

where the plastic multiplier parameters $\overline{\lambda}_u$ and $\overline{\lambda}_v$ have been introduced to participate in evolution equations obtained from Kuhn-Tucker optimality conditions [6]. The constitutive equations for the elastoplastic case are

$$
\dot{N} = \begin{cases} EA\dot{\varepsilon}; & \dot{\overline{\lambda}}_u = 0 \\ \frac{EA\overline{K}_u}{EA+\overline{K}_u}\dot{\varepsilon}; & \dot{\overline{\lambda}}_u > 0 \end{cases}, \quad
\dot{T} = \begin{cases} GA\dot{\gamma}; & \dot{\overline{\lambda}}_v = 0 \\ \frac{GA\overline{K}_v}{GA+\overline{K}_v}\dot{\gamma}; & \dot{\overline{\lambda}}_v > 0. \end{cases}
\tag{33}
$$

Accompanying loading/unloading conditions and consistency condition obey $\dot{\lambda}\Phi = 0, \dot{\lambda} \geq 0, \Phi \leq 0, \dot{\lambda}\dot{\Phi} = 0$.

Once the ultimate failure point is reached, enhanced kinematics needs to be activated. All further plastic deformation will be accumulated at the discontinuity section, that once passed the peak resistance. The corresponding strain fields containing regular and singular components are obtained:

$$
\begin{aligned}
\varepsilon &= \overline{\varepsilon} + \overline{\overline{\varepsilon}} = \overline{\varepsilon}^e + \overline{\varepsilon}^p + \overline{\overline{\varepsilon}} \\
\gamma &= \overline{\gamma} + \overline{\overline{\gamma}} = \overline{\gamma}^e + \overline{\gamma}^p + \overline{\overline{\gamma}}.
\end{aligned}
\tag{34}
$$

The failure criteria for mode I and mode II failure are defined as

$$
\begin{aligned}
\overline{\overline{\Phi}}_u\left(t_u, \overline{\overline{q}}_u\right) &= t_u - \left(N_u - \overline{\overline{q}}_u\right) \leq 0 \\
\overline{\overline{\Phi}}_v\left(t_v, \overline{\overline{q}}_v\right) &= |t_v| - \left(T_u - \overline{\overline{q}}_v\right) \leq 0,
\end{aligned}
\tag{35}
$$

where N_u, T_u are the ultimate capacity forces and $\overline{\overline{q}}_u$, $\overline{\overline{q}}_v$ are stress-like softening variables which increase exponentially as

$$
\begin{aligned}
\overline{\overline{q}}_u &= N_u \left(1 - exp \left(-\overline{\overline{\xi}}_u \frac{N_u}{G_{f,u}} \right) \right) \\
\overline{\overline{q}}_v &= T_u \left(1 - exp \left(-\overline{\overline{\xi}}_v \frac{T_u}{G_{f,v}} \right) \right),
\end{aligned}
\tag{36}
$$

and t_u, t_v are traction forces at the discontinuity obtained from equilibrium equations (26). The evolution of internal variables in softening states

$$
\begin{aligned}
\dot{\alpha}_u &= \dot{\overline{\overline{\lambda}}}_u \frac{\partial \overline{\overline{\Phi}}_u}{\partial N} = \dot{\overline{\overline{\lambda}}}_u sign(N); \quad \dot{\overline{\overline{\xi}}}_u = \dot{\overline{\overline{\lambda}}}_u \frac{\partial \overline{\overline{\Phi}}_u}{\partial \overline{\overline{q}}_u} = \dot{\overline{\overline{\lambda}}}_u \\
\dot{\alpha}_v &= \dot{\overline{\overline{\lambda}}}_v \frac{\partial \overline{\overline{\Phi}}_v}{\partial T} = \dot{\overline{\overline{\lambda}}}_v sign(T); \quad \dot{\overline{\overline{\xi}}}_v = \dot{\overline{\overline{\lambda}}}_v \frac{\partial \overline{\overline{\Phi}}_v}{\partial \overline{\overline{q}}_v} = \dot{\overline{\overline{\lambda}}}_v,
\end{aligned}
\tag{37}
$$

where $\overline{\overline{\lambda}}$ is the plastic multiplier associated with the softening behaviour and α is an equivalent to the accumulated plastic strain at the discontinuity.

2.4 The Finite Element Equations of a Coupled Poroplastic Problem

In this section, the final finite element implementation aspects accounting for each single element contribution, further denoted with subscript e, are presented.

The regular part of weak form (24/1) leads to the element residual equation

$$
\mathbf{r}_d = \mathbf{F}^{ext} - \mathbf{A}_{e=1}^{n_{el}} \int_0^{l_e} \mathbf{B}^{d,T} \boldsymbol{\sigma} \, dx,
\tag{38}
$$

where the total stress resultants $\boldsymbol{\sigma}$ are obtained in terms of effective stress resultants $\boldsymbol{\sigma}'$ and pore pressures $\mathbf{p}$ in (8). The symbol $\mathbf{A}_{e=1}^{n_{el}}$ denotes the finite element assembly operator for all element contributions. The effective stress resultants $\boldsymbol{\sigma}'$ are calculated in terms of regular parts of enhanced strain field (23). The enhanced strain parameters $\boldsymbol{\alpha}$, in each element where localization occurs, are obtained by solving the local equilibrium of the effective stresses

$$
\mathbf{h}^{(e)} = \int_0^{l_e} \overline{\mathbf{G}} \boldsymbol{\sigma}' \, dx + \mathbf{t}',
\tag{39}
$$

where $\mathbf{t}'$ represent the corresponding effective tractions acting at the discontinuity. The local equilibrium equation in (39) offers the benefit of local computation of the enhanced parameters. Subsequent static condensation of these parameters allows

to keep standard matrix at the global level. The local computation algorithm and numerical procedure are described in the next subsection.

Upon introducing the finite element interpolations, the coupled fluid equation (10) results with the finite element residual form

$$\mathbf{r}_p = \mathbf{Q}^{ext} - \mathbf{A}_{e=1}^{n_{el}} \left[\int_0^{l_e} \mathbf{N}^{p,T} M^{-1} \mathbf{N}^p dx \dot{\mathbf{p}}_e - \right.$$
$$\left. - \int_0^{l_e} \mathbf{N}^{p,T} \alpha \mathbf{B}^d dx \dot{\mathbf{d}}_e - \int_0^{l_e} \mathbf{B}^{p,T} k_f \mathbf{B}^p dx \mathbf{p}_e \right], \tag{40}$$

where $\mathbf{Q}^{ext}$ represent the external applied fluxes and imposed pressures. The consistent linearization of the Eqs. (38) and (40) leads to a set of linear algebraic equations

$$\mathbf{r}_d^{(i)} - \mathbf{A}_{e=1}^{n_{el}} \left[\mathbf{K}_e \Delta \mathbf{d}_e - \mathbf{L}_e \Delta \alpha_e - \mathbf{Q}_e \Delta \mathbf{p}_e \right] = 0 \tag{41}$$

and

$$\mathbf{r}_p^{(i)} - \mathbf{A}_{e=1}^{n_{el}} \left[\frac{1}{\Delta t} \mathbf{Q}_e^T \Delta \mathbf{d}_e + \left(\mathbf{H}_e + \frac{1}{\Delta t} \mathbf{S}_e \right) \Delta \mathbf{p}_e \right] = 0 \tag{42}$$

in the increments $\Delta t = t_{n+1}^{(i+1)} - t_{n+1}^{(i)}$, where (i) denotes iteration counter within the time interval $[t_n, t_{n+1}]$. The matrices are evaluated in the previous iteration (i) where all values are known. The element stiffness matrix $\mathbf{K}_e$ is defined as

$$\mathbf{K}_e = \int_0^{l_e} \mathbf{B}^{d,T} \mathbf{D}_{sk} \mathbf{B}^d dx \tag{43}$$

and the localized contribution matrix

$$\mathbf{L}_e = \int_0^{l_e} \mathbf{B}^{d,T} \mathbf{D}_{sk} \overline{\mathbf{G}} dx. \tag{44}$$

The compressibility matrix $\mathbf{S}_e$, the permeability matrix $\mathbf{H}_e$ and the coupling matrix $\mathbf{Q}_e$ are given by

$$\mathbf{S}_e = \int_0^{l_e} \mathbf{N}^{p,T} M^{-1} \mathbf{N}^p dx, \tag{45}$$

$$\mathbf{H}_e = \int_0^{l_e} \mathbf{B}^{p,T} k_f \mathbf{B}^p dx, \tag{46}$$

$$\mathbf{Q}_e = \int_0^{l_e} \mathbf{B}^{d,T} b \mathbf{N}^p dx. \tag{47}$$

The linearization of local equilibrium equation in (39) results with

$$\mathbf{h}_e^{(i)} - \mathbf{L}_e^T \Delta \mathbf{d}_e - \mathbf{F}_e \Delta \boldsymbol{\alpha}_e = 0, \tag{48}$$

where

$$\mathbf{F}_e = \int_0^{l_e} \overline{\mathbf{G}}^T \mathbf{D}_{sk} \overline{\mathbf{G}} + \mathbf{K}_{dis}. \tag{49}$$

Matrix $\mathbf{K}_{dis}$ contains consistent tangent stiffness components for the discontinuity obtained as a derivatives of the exponential softening laws from (36) with respect to the corresponding displacement jumps.

The enhanced strain parameters $\Delta\boldsymbol{\alpha}$ can be obtained by the local operator split solution procedure and return mapping algorithm presented in the next section. Finally, the static condensation strategy serves for local elimination of the enhanced strain parameters which leads to the final statically condensed equation

$$\mathbf{r}_d^{(i)} - \mathbf{A}_{e=1}^{n_{el}} \left[\left(\mathbf{K}_e - \mathbf{L}_e^T \mathbf{F}_e^{-1} \mathbf{L}_e \right) \Delta \mathbf{d}_e - \mathbf{Q}_e \Delta \mathbf{p}_e \right] = 0. \tag{50}$$

2.5 The Operator Split Algorithm

The operator split is an element-wise algorithm performed for each directional component with its ultimate goal of computing the internal variables related to discontinuity. After computing the internal variables locally, the global solution procedure with Newton incremental/iterative procedure can be performed.

It is assumed that the best iterative value of displacements $u_{n+1}^{(i)}$ and $v_{n+1}^{(i)}$ for which the trial values of the traction forces are obtained

$$t_{*,n+1}^{trial} = -\int_0^{l_e} \overline{G} \left[EA \left(\sum_{a=1}^2 B_a^d u_{a,n+1}^{(i)} + \overline{G} \alpha_{*,n} \right) \right] \tag{51}$$

where $\alpha_{*,n}$ represents the discontinuity parameters at previous time for softening plastic deformation. The * denotes each directional component of the Timoshenko beam. Later on, the trial value of failure functions ought to be calculated

$$\overline{\overline{\Phi}}_{*,n+1}^{trial} = t_{*,n+1}^{trial} - \left(N_u - \overline{\overline{q}}_{*,n} \right). \tag{52}$$

If the trial values of the failure functions are negative or zero, the elastic trial step is accepted for final, with no modification of the plastic strain from the previous time step

$$\alpha_{*,n+1} = \alpha_{*,n}; \ \overline{\overline{\xi}}_{*,n+1} = \overline{\overline{\xi}}_{*,n}, \tag{53}$$

The plastic softening parameter will remain intact, while the traction force will be changed due to displacement increment.

On the other hand, if the trial values of failure functions are positive, the current step is in the softening plasticity and there is a need to modify the elastic strain and internal variables $\alpha_{*,n}$, in order to re-establish the plastic admissibility at discontinuity. The internal softening plasticity variables ought to be updated by using evolution equations

$$\alpha_{*,n+1} = \alpha_{*,n} + \bar{\bar{\lambda}}_{*,n+1} sign\left(t_{*,n+1}^{trial}\right) \tag{54}$$

and

$$\bar{\bar{\xi}}_{*,n+1} = \bar{\bar{\xi}}_{*,n} + \bar{\bar{\lambda}}_{*,n+1} \tag{55}$$

where $\bar{\bar{\lambda}}_{*,n+1}, \bar{\bar{\lambda}}_{*,n+1}$ are softening plastic multipliers. The value of the plastic multiplier is determined from the conditions $\bar{\bar{\Phi}}_{*,n+1} \leq tol$ and the solutions of a nonlinear equations are obtained iteratively using the Newton-Raphson method

$$\bar{\bar{\Phi}}_{*,n+1} = \bar{\bar{\Phi}}_{*,n+1}^{trial} + \left(\bar{\bar{q}}_{*,n+1} - \bar{\bar{q}}_{*,n}\right) + EA\bar{G}\bar{\bar{\lambda}}_{*,n+1} \leq tol \tag{56}$$

In the plastic softening step, the traction forces are produced by a change of discontinuity parameters α_*.

3 Numerical Simulations

In this section, the numerical simulations for several numerical tests are presented. The uniaxial tension and compression tests are performed on heterogeneous 2D rock specimens. The influence of heterogeneity with different distributions of phase I and II (strong and weak phase) are studied. Fluid-saturated rock sample with localized shear band formation development is presented as well. Presented numerical model formulations are implemented into the research version of the computer code FEAP [32].

3.1 Preparation of 2D Plain Strain Rock Specimens

2D plane strain rock specimens are constructed. The specimens are of dimensions 10×10 cm (with unit thickness) and are meshed with triangles by means of Delaunay algorithm. The specimen has 253 nodes and 704 elements (Fig. 7). Timoshenko beam elements are positioned on each edge of every triangle in the specimen. Their geometric properties represent the corresponding part in specimen volume. The main hypothesis in constructing the lattice model is that the cells connected by cohesive
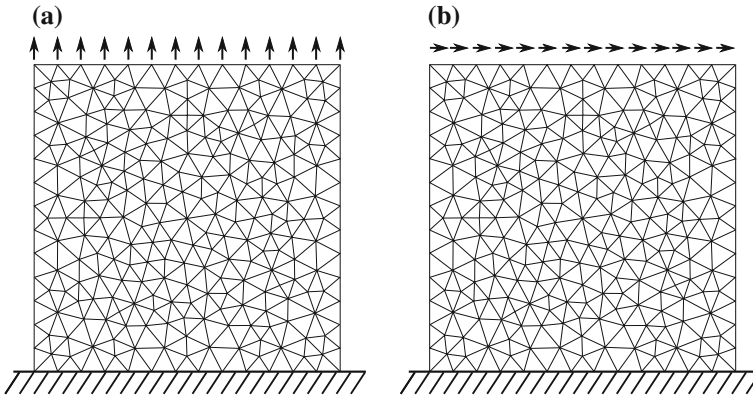
Fig. 7 A homogeneous 2D plain strain specimen is constructed. Uniaxial tension (**a**) and shear test (**b**) are performed in linear elastic regime to validate the model

links (beams) correspond to the representative part of the specimen which have homogeneous properties, while the heterogeneities are introduced through the cohesive links. Thus, the Voronoi cells are derived from Delaunay triangulation and the beam cross sections are computed from the length of the common size of the neighbouring cells (Fig. 8). The material parameters are taken the same as in the equivalent standard continuum.

In order to validate the lattice model parameters, the tension and shear tests are conducted in the linear elastic regime on the proposed homogeneous specimen (shown in Fig. 7) in two versions: lattice model and equivalent standard continuum model with triangular solid elements. The material parameters are the same for each test version: $E = 1000 \, \text{kN/cm}^2$, $\nu = 0.2$. The results are presented in Fig. 9a, b.

The equivalent standard continuum model (with triangles as finite elements) operate only in linear elastic regime and its response matches with linear elastic regime of lattice models before the failure phase, showing that the proposed model is capable of reproducing classical linear elastic continuum with such computed lattice parameters.

Fig. 8 Beam cross sections are computed from the length of the common size of the neighbouring cells
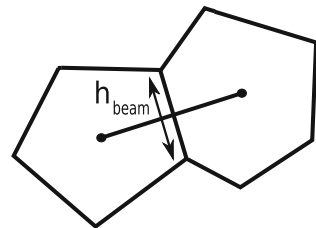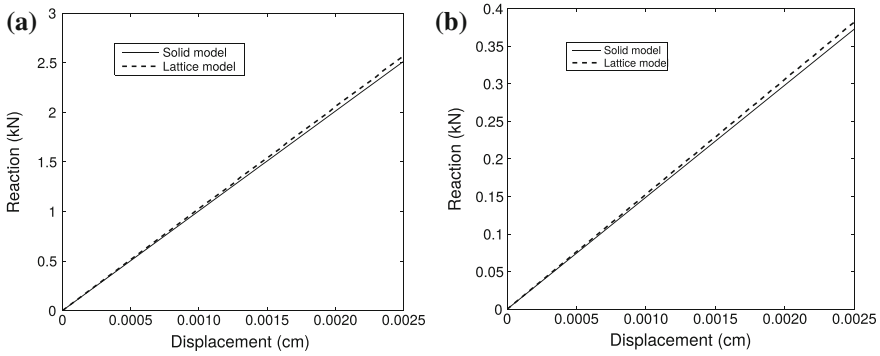
Fig. 9 Response of homogeneous specimen in linear elastic regime for **a** tension test and **b** shear test in two versions: solid model with triangles and lattice model

3.2 Influence of Heterogeneity in Tension and Compression Tests

In this example, the influence of heterogeneity on a global response is studied. Three different specimens with the same geometric properties (same specimen size), but different levels of heterogeneity are subjected to uniaxial tension and compression tests. Table 1 summarizes the mechanical and geometric characteristics of the specimen used for these experiments. The corresponding macroscopic results are shown in Fig. 10a, b.

The specimens are given different initial properties, specifically with 40, 50 and 60 % of phase II material. With an increase of phase II material, the global modulus of elasticity decreases. This is the result of more elements of phase II representing initial weaker material, which makes the global response of specimen more ductile and also with a somewhat lower value of modulus of elasticity. However, it can also be seen from global exponential curve that, when a ratio of phase II material increases, the failure of the specimen becomes more ductile in fracture process zone creation, but also more brittle in the softening response phase, for when the fracture

Table 1 Mechanical and geometric characteristics of the specimen

Phase I	Phase II
$E = 7000\,\text{kN/cm}^2$	$E = 1000\,\text{kN/cm}^2$
	$v = 0.2$
$v = 0.2$	$\sigma_u = 2.2\,\text{MPa},\ \tau_u = 1.15\,\text{MPa}$
Tension fr. energ.:	$G_f^{(u)} = 10\,\text{N/m},$
	$G_f^{(v)} = 1.5\,\text{N/m}$
Comp. fr. energ.:	$G_f^{(u)} = 350\,\text{N/m},$
	$G_f^{(v)} = 10\,\text{N/m}$
Dimensions: $0.1 \times 0.1 \times 0.01$ m; 40, 50, 60 % phase II	
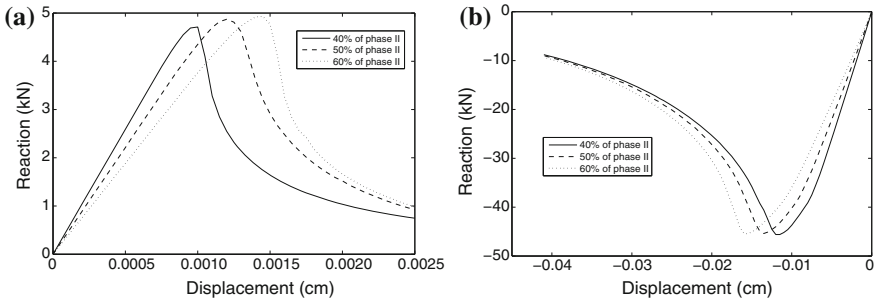
Fig. 10 The computed macroscopic response with different levels of heterogeneity for: **a** uniaxial tension test and **b** uniaxial compression test
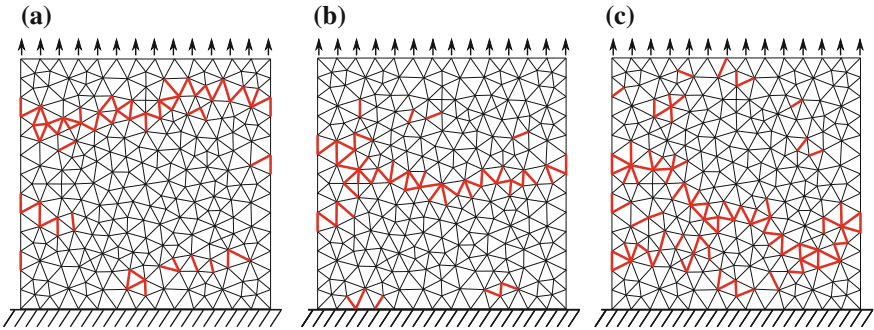
Fig. 11 Final failure patterns created in tension test for specimens with: **a** 40 % of phase II, **b** 50 % of phase II and **c** 60 % of phase II (broken links are *red coloured*) (Color Online)

starts the complete failure happens faster. This is due to appearance of many more potential macro-cracks, which drives more quickly the stress to zero.

The failure patterns of three different heterogeneous specimens are shown in Figs. 11 and 12. Figure 11 presents the final macro-cracks at the end of tension test computations for the specimens with 40, 50 and 60 % of phase II material. It is observed that one dominant macro-crack is present in all of the specimens inducing the final failure mechanism. However, in each specimen the macro-crack formed differently depending on the initial heterogeneity which decides the crack path. Failure due to mode I is more pronounced in tension test.

The ultimate shear strength is defined by the Mohr-Coulomb failure criterion

$$\tau_f = \tau_u + \sigma_c \cdot \tan(\phi), \tag{57}$$

where τ_u represents cohesion-like value of ultimate shear force when compression force is equal to zero, σ_c represents the compression force and ϕ is internal angle of friction. Figure 12 reveals the final cracks formed at the end of compression tests where not only one macro-crack is enough to break the specimens. Contrary to
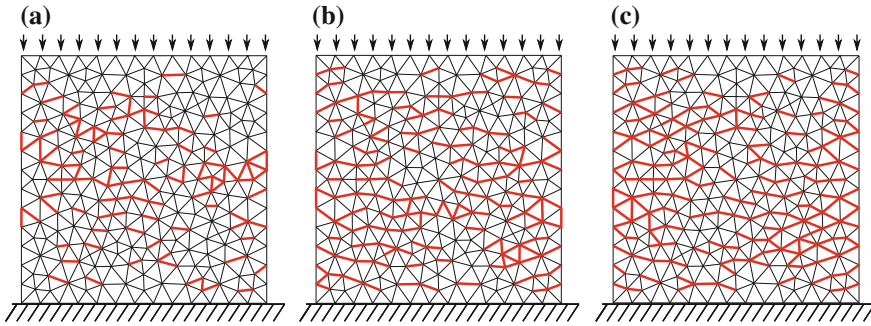
Fig. 12 Final failure patterns created in compression test for specimens with: **a** 40 % of phase II, **b** 50 % of phase II and **c** 60 % of phase II (broken links are *red coloured*) (Color Online)

tension test crack patterns, in compression test much more macro-cracks are needed to drive the specimens to failure and these are influenced more by mode II mechanism, compared to tension test, which forms the final crack patterns together with mode I. It is important to note that red coloured links in Figs. 11 and 12 represent the failed cohesive links. However, the actual cracks are localized inside elements and enable the crack propagation between the Voronoi cells, which are dual to Dealunay triangulation.

In either tension or compression, the difference in reduction of the peak stresses in different specimens remains fairly mild. Having approximately the same peak resistance is quite realistic to expect for the similar failure pattern is created once the threshold is reached. However, the similar peak stresses in compression test leads to conclusion that despite the variations in heterogeneity, crack propagation patterns in each of the samples remain similar with similar failure mechanism present in all of them, which can be observed in Fig. 12. Specifically, this means that more defects were present in the specimens with more phase II material which made the material softer, but at the same time these were not crucial for complete failure which was caused by similar macro-cracks in all specimens. This leads to conclusion that difference in heterogeneity, that was used here: 40, 50, 60 % of phase II, is not as significant to lead to drastically different values of ultimate stresses.

3.3 Drained Compression Test of the Poro-plastic Sample with the Localized Failure

The fluid saturated rock sample under compression test is considered in this section. The geometry of the sample and boundary conditions imposed on the displacement and pore pressure fields are shown in Fig. 13. The external load is applied via constant velocity $v_0 = 5 \times 10^{-4}$ m/s imposed on the top base. With the aim of observing the coupling effects as well, the tests are then repeated with the imposed constant velocity

Fig. 13 Geometry of the poroplastic sample and imposed boundary conditions
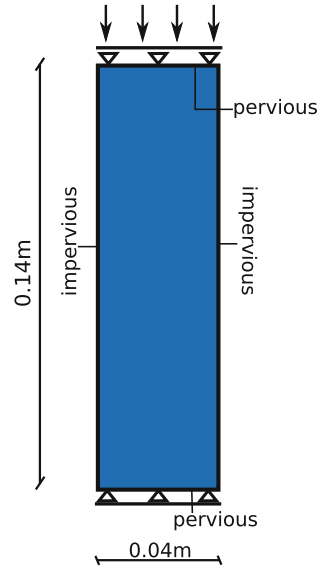
$v_0 = 1.5 \times 10^{-3}$ m/s. The chosen material parameters listed in Table 2 correspond to the limestone fully saturated with the water. The value of hydraulic permeability of the sample obtained from the parameters in the Table 2 is equal to $K_h = \rho_w g K_f = 1 \times 10^{-8}$ m/s, where the procedure of computing lattice permeabilities is used. Such procedure is performed to find equivalent permeabilities when the fluid flows across

Table 2 Material parameters considered in the numerical simulations of poro-plastic sample

Drained Young modulus	$E_{sk} = 50$ GPa
Drained Poisson ratio	$\nu_{sk} = 0.25$
Tensile yield stress	$\sigma_{y,t} = 12$ MPa
Shear yield stress	$\tau_y = 23$ MPa
Hardening modulus	$\overline{K} = 5$ GPa
Tensile strength	$\sigma_{u,t} = 13$ MPa
Shear strength	$\tau_u = 25$ MPa
Angle of friction	$\phi = 35°$
Fracture energies	$G_{f,u} = 300$ N/m; $G_{f,v} = 600$ N/m
Biot coefficient	$b = 0.8$
Biot modulus	$M = 16.9$ GPa
Porosity	$n_f = 0.1$
Permeability	$K_f = 1 \times 10^{-9}$ m^2/(kPa/s)
Fluid density	$\rho_w = 1000$ kg/m^3

the discrete lattice network. Associating K_f with given permeability and k_f with lattice permeability, the following expression is obtained

$$k_f = \frac{K_f}{c}, \tag{58}$$

with $c = h_f / l_e$ being the coefficient of modification of permeability for given lattice. Here, h_f denotes the shortest distance between the two centroids of neighbouring triangles and l_e is the length of given element. See [31] for more elaborate explanation of this procedure.

The final goal is to investigate the influence of heterogeneity upon the localized failure of the proposed sample. The presented discrete model formulation is capable of considering the influence of heterogeneity. Here, the two-phase representation is adopted, where the second phase takes the slightly weaker properties in terms of material strengths ($\sigma_{u,t} = 12\,\mathrm{MPa}$; $\tau_u = 24\,\mathrm{MPa}$). The two-phases are distributed randomly throughout the sample and each phase participates with equal number of elements. The differences in two samples are brought by the different distributions of the phases when the random sampling is performed two times in a row. Figures 14 and 15 show the displacements and pore pressures of the heterogeneous samples 1 and 2 plotted in the deformed mesh at the final time step of the simulation. These results are obtained with the imposed constant velocity of $v_0 = 5 \times 10^{-4}\,\mathrm{m/s}$. It can be observed from the deformed meshes of both samples that the localized macro cracks propagate differently in two cases only because of the slight difference in initial heterogeneity distributions. Macro-cracks also formed the irregular geometries that propagated through the weaker parts of the material. The main strength of the presented discrete model is in simulating the heterogeneous materials where macro-cracks propagate through the material's weaker phases, avoid the stiffer ones and
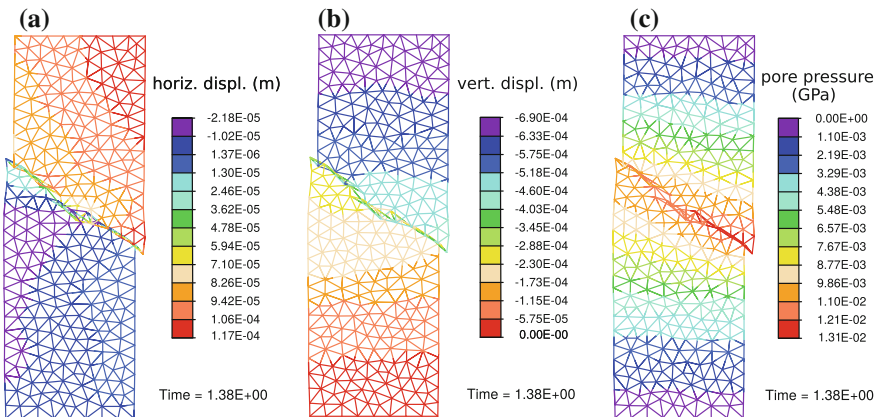
Fig. 14 The state of the 1st heterogeneous sample after the compression test (imposed velocity $v_0 = 5 \times 10^{-4}$ m/s): **a** horizontal displacement **b** vertical displacement **c** pore pressure
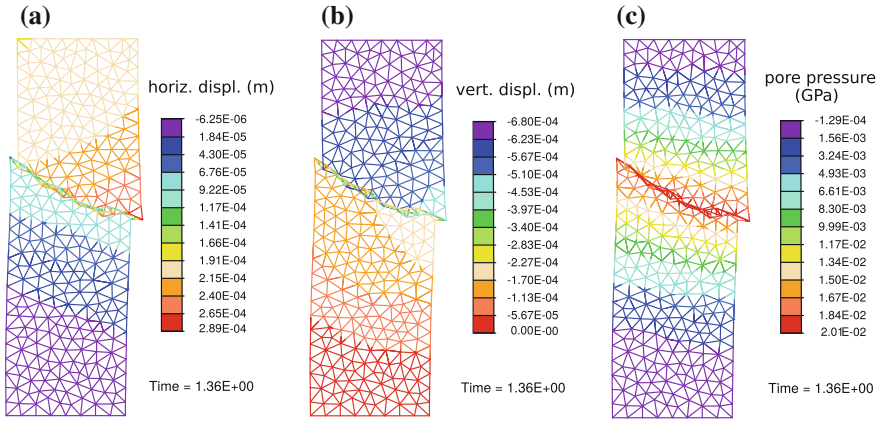
Fig. 15 The state of the 2nd heterogeneous sample after the compression test (imposed velocity $v_0 = 5 \times 10^{-4}$ m/s): **a** horizontal displacement **b** vertical displacement **c** pore pressure

exhibit the irregular geometries. When it comes to the pore pressures, previoussides and reach their highest values near the localized zone.

To investigate the coupling effects, the two heterogeneous samples are put under compression test with a different rate of imposed vertical displacement on the top base $v_0 = 1.5 \times 10^{-3}$ m/s. The macroscopic curves including the cumulative vertical reaction and pore pressure in the centre of the sample in the close neighboured of the localized zone are presented in Fig. 16, for two heterogeneous samples and different imposed velocities obtained within the compression tests.

The macroscopic vertical reactions indicate that higher rates of imposed displacement cause the samples to be more resistant (larger ultimate stress) and more ductile
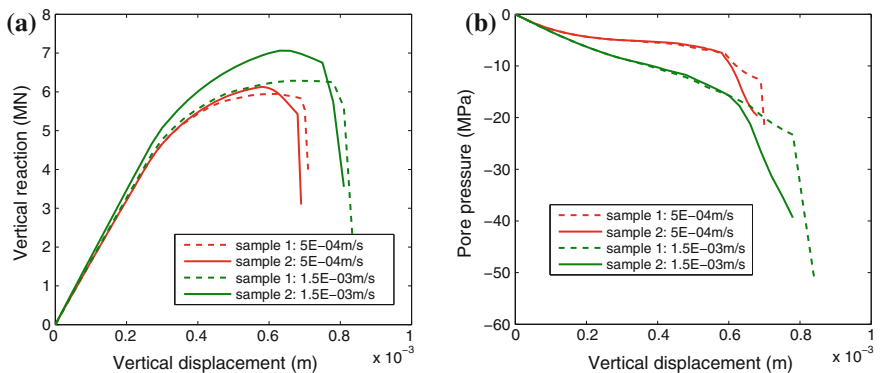
Fig. 16 Macroscopic curves of the poro-plastic sample obtained within the compression test **a** cumulative vertical reaction versus impose displacement **b** pore pressure at the sample centre versus imposed displacement
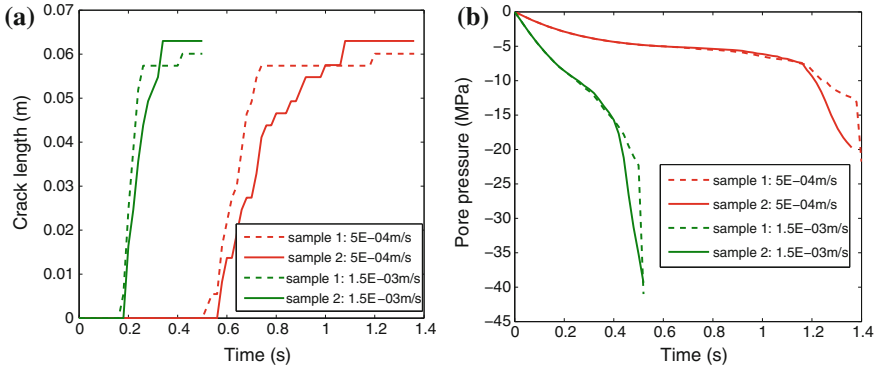
Fig. 17 **a** Crack length versus time **b** pore pressure at the sample centre versus time

(larger displacement is needed to drive the samples to the failure). This is due to an increase of pore pressure which is brought by shorter time left for drainage at the sample centre (Fig. 16b).

The pronounced coupling effects are more obvious when it comes to the non-linear behaviour and formation of localization zone. In the beginning of the test, the vertical reaction is less influenced by higher pore pressure.

No coupling effect is observed in the geometry of the macro-crack for each sample when it comes to the localized zone formation. More precisely, the discontinuity still propagated through the same elements for different imposed velocities.

The differences with respect to heterogeneities seem to increase in the nonlinear zone with the higher imposed velocity. Namely, the increase of flow through cracks in localization zone, together with the 'faster' loading, induces the higher rates of pore pressures making the heterogeneities' influence even more profound.

As can be seen from Fig. 17a, where time history of the crack length is presented, cracks start to propagate at some point in time when the external load produces significant stress triggering the crack. The cracks then propagate quickly through the samples. The plots for samples with applied faster external load ($v_0 = 1.5 \times 10^{-3}$ m/s) show, that in these cases, cracks propagate more quickly and the tests are completed in less time. Figure 17b presents the time evolution of pore pressure in the centre of the sample and in the close neighboured of the crack, showing the shorter time needed for completion of test and faster rate of the pore pressure increase.

4 Conclusions

In this chapter the discrete element modelling suitable for describing the fracture process with localized failure zones in heterogeneous non-saturated and fully fluid-saturated poro-plastic medium is presented, where coupling between the fluid and

solid obey the Biot theory of poroplasticity. The localized failure mechanisms are incorporated through the enhanced kinematics of Timoshenko beams that act as cohesive links between the grains of heterogeneous rock material. The embedded discontinuities can represent the failure modes I and II, as well as their combination. The fluid flow is governed by the Darcy law with assumed continuous pore pressure field.

The model ingredients are incorporated into the framework of embedded discontinuity finite element method, where the computation of the enhanced discontinuity parameters requires only local element equilibrium. Further use of the static condensation of the enhanced parameters at the element level, leads to the computationally very efficient approach and numerical implementation that fits within the standard finite element code architecture.

The main strength of the proposed discrete model lies in its ability to account for material heterogeneities with localized macro-cracks propagating throughout the weaker parts of the material and forming the irregular geometries. Such a phenomenon is presented by the numerical simulations of two samples with equal geometries and material properties, but slightly different distribution of material heterogeneities throughout samples, which present different behaviour in terms of localized macro-crack propagation. The solid-fluid coupling plays important role here as well, bringing the variations in macroscopic responses and compliance of the samples. It is important to emphasise that heterogeneous effects become more pronounced with the coupling effects and higher rates of the imposed velocities.

References

1. Terzaghi, K.: Theoretical Soil Mechanics. Wiley (1943)
2. Biot, M.A.: Mechanics of incremental deformations. John Wiley & Sons (1965)
3. Lewis, R.W., Schrefler, B.A.: The Finite Element Method in the Static and Dynamic Deformation and Consolidation of Porous Media. Wiley, Chichester, 2nd edition (1998)
4. Zienkiewicz, O.C., Taylor, R.L: Finite Element Method. Butterworth-Heinemann, 5th edition (2000)
5. Bathe, K.: Finite Element Procedures. Prentice Hall, New Jersey (2006)
6. Ibrahimbegovic, A.: Nonlinear Solid Mechanics: Theoretical Formulations and Finite Element Solution Methods. Springer (2009)
7. Simo, J.C., Oliver, J., Armero, F.: An analysis of strong discontinuities induced by strain-softening in rate-independent inelastic solids. Comput. Mech. **12**, 277–296 (1993)
8. Simo, J.C., Rifai, M.S.: A class of mixed assumed strain methods and the method of incompatible modes. Int. J. Numer. Meth. Engng. **29(8)**, 1595–1638 (1990)
9. Ortiz, M., Leroy, Y., Needleman, A.: A finite element method for localized failure analysis. Comput. Methods Appl. Mech. Engrg. **61**, 189–214 (1987)
10. Ibrahimbegovic, A., Melnyk, S.: Embedded discontinuity finite element method for modeling of localized failure in heterogeneous materials with structured mesh: an alternative to extended finite element method. Comput. Mech. **40**, 149–155 (2007)
11. Moes, N., Dolbow, J., Belytschko, T.: A finite element method for crack growth without remeshing. Int. J. Numer. Meth. Engng. **46**, 131–150 (1999)
12. Fries, T.P., Belytschko, T: The intrinsic XFEM: a method for arbitrary discontinuities without additional unknowns. Int. J. Numer. Meth. Engng. **68**, 1358–13850 (2006)

13. Fries, T.P., Belytschko, T: The extended/generalized finite element method: An overview of the method and its applications. Int. J. Numer. Meth. Engng. **84**, 253–304 (2010)
14. Rethore, J., de Borst, R., Abellan, M.A: A two-scale approach for fluid flow in fractured porous media. Int. J. Numer. Meth. Engng. **71**, 780–800 (2007)
15. Rethore, J., de Borst, R., Abellan, M.A: A two-scale model for fluid flow in an unsaturated porous medium with cohesive cracks. Comput. Mech. **42**, 227–238 (2008)
16. de Borst, R., Rethore, J., Abellan, M.A: A numerical approach for arbitrary cracks in a fluid-saturated medium. Arch. Appl. Mech. **75**, 595–606 (2006)
17. Benkemoun, N., Gelet, R., Roubin, E., Colliat, J.B.: Poroelastic two-phase material modeling: theoretical formulation and embedded finite element method implementation. Int. J. Numer. Anal. Meth. Geomech. **39**, 1255–1275 (2015)
18. Callari, C., Armero, F.A.: Finite element methods for the analysis of strong discontinuities in coupled poro-plastic media. Comput. Methods Appl. Mech. Engrg. **191**, 4371–4400 (2002)
19. Callari, C., Armero, F., Abati, A.: Strong discontinuities in partially saturated poroplastic solids. Comput. Methods Appl. Mech. Engrg. **199**, 1513–1535 (2010)
20. Schrefler, B.A., Secchi, S., Simoni, L.: On adaptive refinement techniques in multi-field problems including cohesive fracture. Comput. Methods Appl. Mech. Engrg. **195**, 444–461 (2006)
21. Secchi, S., Schrefler, B.A.: A method for 3D hydraulic fracturing simulation. Int. J. Fract. **178**, 245–258 (2012)
22. Nikolic, M., Ibrahimbegovic, A., Miscevic, P.: Brittle and ductile failure of rocks: Embedded discontinuity approach for representing mode i and mode ii failure mechanisms. Int. J. Numer. Meth. Engng. **102**, 1507–1526 (2015)
23. Nikolic, M., Ibrahimbegovic, A.: Rock mechanics model capable of representing initial heterogeneities and full set of 3d failure mechanisms. Comput. Methods Appl. Mech. Engrg. **290**, 209–227 (2015)
24. Ostoja-Starzewski, M.: Lattice models in micromechanics. Appl. Mech. Rev. **55**, 35–60 (2002)
25. Cusatis, G., Bazant, Z., Cedolin, L.: Confinement-shear lattice CSL model for fracture propagation in concrete. Comput. Methods Appl. Mech. Engrg. **195**, 7154–7171 (2006)
26. Vassaux, M., Richard, B., Ragueneau, F., Millard, A., Delaplace, A.: Lattice models applied to cyclic behavior description of quasi brittle materials: advantages of implicit integration. Int. J. Numer. Anal. Meth. Geomech. **39**, 775–798 (2015)
27. Karihaloo, B., Shao, P., Xiao, Q.: Lattice modelling of the failure of particle composites. Eng. Fract. Mech. **70**, 2385–2406 (2003)
28. Bui, N., Ngo, M., Nikolic, M., Brancherie, D., Ibrahimbegovic, A.: Enriched timoshenko beam finite element for modeling bending and shear failure of reinforced concrete frames. Comput. Struct. **143**, 9–18 (2014)
29. Jukic, M., Brank, B., Ibrahimbegovic, A.: Embedded discontinuity finite element formulation for failure analysis of planar reinforced concrete beams and frames. Eng. Struct. **50**, 115–125 (2013)
30. Pham, B., Brancherie, D., Davenne, L., Ibrahimbegovic, A.: Stress-resultant models for ultimate load design of reinforced concrete frames and multi-scale parameter estimates. Comput. Mech. **51**, 347–360 (2013)
31. Nikolic, M., Ibrahimbegovic, A., Miscevic, P.: Discrete element model for the analysis of fluid-saturated fractured poro-plastic medium based on sharp crack representation with embedded strong discontinuities. Comput. Methods Appl. Mech. Engrg. **298**, 407–427 (2016)
32. Taylor R.L.: FEAP - A Finite Element Analysis Program, University of California at Berkeley